

# 000 001 002 003 004 005 WHEN MLLMS MEETS COMPRESSION DISTORTION: 006 A CODING PARADIGM TAILORED TO MLLMS 007 008 009

010 **Anonymous authors**  
011 Paper under double-blind review  
012  
013  
014  
015  
016  
017  
018  
019  
020  
021  
022  
023  
024  
025  
026  
027  
028

## ABSTRACT

029  
030 The increasing deployment of powerful Multimodal Large Language Models  
031 (MLLMs), typically hosted on cloud platforms, urgently requires effective com-  
032 pression techniques to efficiently transmit signal inputs (e.g., images, videos)  
033 from edge devices with minimal bandwidth usage. However, conventional image  
034 codecs are optimized for fidelity to serve the Human Visual System (HVS) and ill-  
035 suited for MLLMs, in which diverse downstream tasks are jointly considered. In  
036 this paper, we first systematically analyze the impact of compression artifacts on  
037 several mainstream MLLMs. We find that: *Compression distortion unevenly im-  
038 pacts different-level image features, leading to varying effects on MLLMs' down-  
039 stream tasks depending on their feature-level reliance.* Motivated by this discov-  
040 ery, we propose an image Codec TAilored to MLLMs (CoTAM) designed to adap-  
041 tively protect multi-level features and suit different demands of downstream tasks.  
042 The encoder leverages CLIP's shallow-layer attention to generate an importance  
043 map for bit allocation, preserving critical semantic regions. Concurrently, the de-  
044 coder integrates a lightweight adapter with a multi-level loss function to ensure  
045 the faithful reconstruction both of low-level details and high-level semantic con-  
046 text for robust synthesis of cross-level features. Extensive experiments validate  
047 that our method achieves up to 35.99% bitrate saving while maintaining the same  
048 performance on the MLLM tasks, outperforming previous SOTA neural codecs.  
049

## 1 INTRODUCTION

050 The proliferation of MLLMs, such as GPT-4o Hurst et al. (2024), Gemini Team et al. (2023),  
051 and LLaVA Liu et al. (2023a), has marked a paradigm shift in artificial intelligence, revolution-  
052 izing human-machine interaction, content understanding Li et al. (2023a), and automation Yin et al.  
053 (2024). These models possess an insatiable appetite for high-quality visual data Zhu et al. (2025)  
054 to fuel their powerful capabilities. As MLLM applications become ubiquitous—from real-time vi-  
055 sual question answering on mobile devices to complex scene analysis in cloud-based services—the  
056 demand for transmitting and storing image and video data is growing at an explosive rate. This  
057 surge creates a critical bottleneck: *the conflict between the need for high-fidelity visual input and the*  
058 *constraints of limited communication bandwidth and storage resources.* Consequently, developing  
059 highly efficient compression techniques tailored for this new era is not just beneficial but imperative.

060 However, existing compression techniques are ill-suited for the versatile, open-world nature of  
061 MLLMs. Conventional codecs are engineered for the HVS Wallace (1991); He et al. (2022); Li  
062 et al. (2024c), while Image Coding for Machine (ICM) methods target specific, narrow computer  
063 vision tasks Feng et al. (2022); Chamaïn et al. (2021). This misalignment leads to inconsistent per-  
064 formance across the diverse capabilities of MLLMs. As illustrated in Fig. 1(a)(b), both methods  
065 exhibit erratic performance, excelling in some tasks while failing in others He et al. (2022); Kao  
066 et al. (2025). Fundamentally, these approaches do not address the crucial question of how MLLMs  
067 holistically perceive and are affected by compression artifacts.

068 To address this gap, our work begins with a systematic investigation into this question. Our analysis  
069 reveals a crucial insight: *Compression distortion unevenly impacts different-level image features,*  
070 *leading to varying effects on MLLMs' downstream tasks depending on their feature-level reliance.*  
071 Specifically, as shown in Fig. 1(c)(d), our analysis reveals that: tasks that rely on either low-level  
072 structural features (e.g., large-font OCR) or global high-level semantic features (e.g., overall scene

understanding) both demonstrate relatively robust to compressed distortion. In contrast, tasks requiring a synthesis of cross-level features (e.g., counting objects) are highly susceptible, as compression artifacts disrupt the crucial integration of low-level information into a coherent high-level semantic. Motivated by this finding, we introduce an image Codec TAilored to MLLMs (CoTAM). At the encoder, our codec leverages priors from the shallow layers of a pre-trained CLIP model Radford et al. (2021) to guide rate allocation. At the decoder, a lightweight adapter with the reconstruction prior and a multi-level objective function ensures that both low-level fidelity and high-level perception are faithfully restored. This mechanism resolves the conflicting demands of different task types, ensuring the reconstructed output is faithful to the MLLMs’ needs. The main contributions of this work are summarized as follows:

- We first provide a systematic analysis of MLLM performance under compression, revealing how MLLMs are affected by compression distortion.
- We propose CoTAM whose encoder uses lightweight CLIP-based semantic priors for rate allocation while the decoder uses a multi-level loss and adapter with reconstruction priors to preserve multi-level information.
- Our approach achieve significant bitrate savings while delivering consistently high performance across a wide spectrum of MLLM tasks, and also shows compatibility with high-resolution and video-based MLLM scenarios.

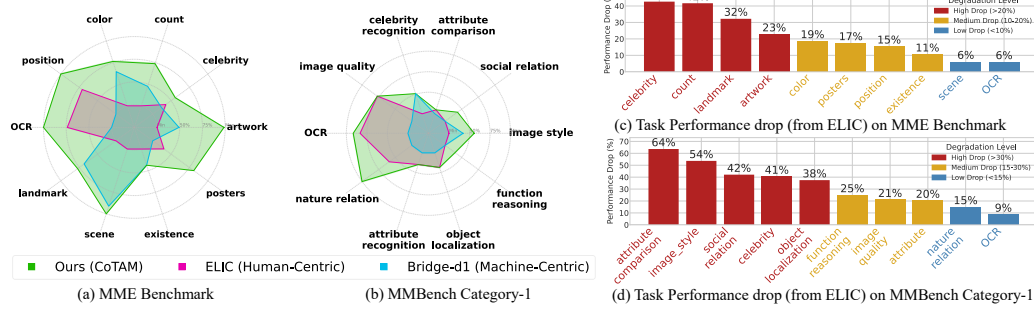


Figure 1: (a)(b) Performance comparison of compression methods on MME Fu et al. (2023) and MMBench Liu et al. (2024b) under similar bitrates. For MMBench, we report the 10 most affected tasks (largest score drops). Human-centric codec ELIC He et al. (2022) excels on low-level structural tasks (e.g., Large-font OCR) and the ICM method Bridge-d1 Kao et al. (2025) excels on high-level tasks (e.g., landmark identification), while our method consistently outperforms both. (c)(d) Compression distortion (from ELIC) affects tasks differently: Tasks relying on either low-level structural features or coarse high-level semantics (e.g., OCR and scene understanding) tend to be relatively robust, whereas those depending on cross-level features (e.g., counting) suffer more, reflecting a synthesis that fails when corrupted low-level information can no longer be coherently structured by the high-level context. Seeing more benchmarks’ sub-tasks and images in Appendix.

## 2 IMPACT ANALYSIS OF IMAGE DISTORTION ON MLLMS

### 2.1 PRELIMINARIES: THE MLLM PIPELINE

The architecture of mainstream MLLMs Li et al. (2024a); Zhu et al. (2025) comprises three key parts: a vision encoder Radford et al. (2021); Zhai et al. (2023), a projector, and a LLM Bai et al. (2023); Touvron et al. (2023). The vision encoder, often a Vision Transformer (ViT) Han et al. (2022), serves as the model’s “eye”, responsible for transforming an input image into a sequence of vision tokens. These vision tokens are then passed through the projector (e.g., some MLP layers), a lightweight network that maps them into the LLM’s feature space. Finally, the LLM backbone (e.g., LLaMA Touvron et al. (2023), Qwen Team (2024)) processes these projected vision tokens alongside a text prompt to perform cross-modal reasoning and generate the final output.

This work investigates the effects of the compression distortion on the Vision Encoder. Because it serves as the sole gateway for visual information into the MLLM, the quality of its output tokens directly dictates the upper bound on the entire model’s downstream performance. To this end, in this

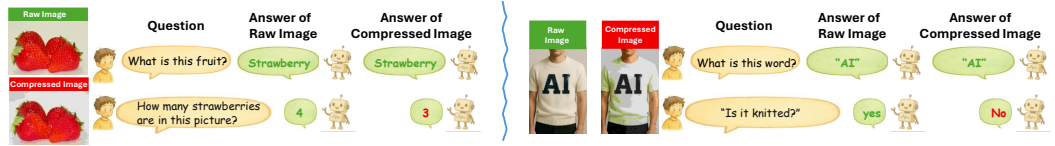


Figure 2: How compression affects VQA tasks: while the MLLM’s robust low-level structural and coarse-grained high-level semantic abilities enable it to identify the “strawberry” and “AI”, it fails on tasks demanding fine-grained cross-level information, such as providing an accurate count.



Figure 3: Information flow across different layers of the vision encoder. According to the flows, we can divide the information processing to three stages as Table 1. In stage 3, a token with high attention no longer represents its own local visual content, but instead transforms into a high-level ‘summary token’ Liu et al. (2025); Li et al. (2023c) responsible for integrating global information.

work, we isolate our analysis from the LLM backbone, whose behavior is conditioned on specific textual prompts, in order to derive general conclusions about the visual processing pipeline itself.

## 2.2 EXPLORING THE IMPACT OF IMAGE COMPRESSION DISTORTION TO MLLMs

To design a codec tailored to MLLMs, we must first understand what visual information MLLMs require and how this information acquisition process is affected by compression artifacts.

### 2.2.1 HOW DOES VISUAL INFORMATION FLOW IN MLLMs?

Prior work shows that weak high-level semantic capability in MLLMs induces hallucinations Fu et al. (2023), whereas supplying richer, clearer image details substantially improves performance Liu et al. (2024a). Together, these findings imply that strong MLLMs must exploit both low-level cues and high-level semantics. A scan of mainstream benchmarks (MME Fu et al. (2023), MMBench Liu et al. (2024b), SEED-Bench Li et al. (2023a)) confirms this breadth: tasks span object recognition and counting, spatial reasoning, OCR, compositional inference, and the interpretation of abstract concepts like emotion and intent. The diversity of these tasks also indicates that *MLLMs rely on visual information across multiple levels of granularity—from low-level pixel details to high-level semantic abstractions*. For example, in Fig. 2, answering “What is the word?” requires low-level structural OCR capabilities, determining “What is this fruit?” demands high-level global semantic reasoning, while the response to “How many strawberries are in this picture?” needs both structural information and global semantics. This raises a pivotal question: *how does the vision encoder transform raw pixels into a feature representation that balances both low-level details and high-level semantics?* To investigate this, we analyze the information flow within the vision encoder (CLIP Radford et al. (2021)), inspired by the inflow/outflow methodology of Tong et al. (2025). Specifically, for a self-attention map  $A \in \mathbb{R}^{N \times N}$  in a given layer, where  $A_{ji}$  denotes the attention from source token  $i$  to target token  $j$ , we define two metrics **Information Inflow & Outflow** to trace the primary information pathways.  $\text{Inflow}(k) = \underset{j}{\operatorname{argmax}} A_{kj}$ , and  $\text{Outflow}(k) = \underset{i}{\operatorname{argmax}} A_{ik}$ .

The visualization of this information flow (Fig. 3) reveals a distinct three-stage feature processing pattern, which is detailed in Table 1 and corroborated by the PCA Maćkiewicz & Ratajczak (1993) visualization and [CLS] attention maps in Fig. 4(a). The process begins with **Stage 1: Preliminary**

162

Table 1: The Three-Stage Pattern of Visual Information Processing in the Vision Encoder.

163

164

165

166

167

168

169

170

171

172

173

174

175

176

177

Stage	Information Flow (Fig. 3)	[CLS] Attention (Fig. 4(a)(b))	PCA-Visualized Features (Fig. 4(c))
<b>Stage 1:</b> Preliminary Screening (Shallow Layers)	<b>Inflow:</b> Receives global guidance from [CLS]. <b>Outflow:</b> Scattered, performs a broad initial screening.	Broad, with higher intensity on key areas.	Resemble raw textures and edges; no significant aggregation.
<b>Stage 2:</b> Local Information Extraction (Middle Layers)	<b>Inflow:</b> Remains anchored to the [CLS] token. <b>Outflow:</b> Concentrates on neighboring patches.	Converges on certain edges and local regions.	Extracts low-level features with clear structures.
<b>Stage 3:</b> Global Semantic Integration (Deep Layers)	<b>Inflow:</b> Diversifies, from [CLS] and summary tokens. <b>Outflow:</b> Disperses again to integrate refined features.	Converges on a few summary tokens.	Extracts cross-level to abstract, high-level semantics; structural details are discarded.

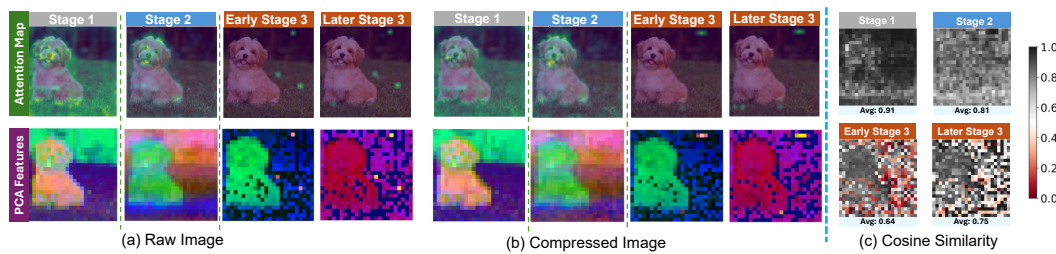


Figure 4: Three stages' CLS attention maps and PCA features in Table 1 (layer 0, 5, 15, 22 in vision encoder) for (a) the raw image and (b) the compressed image. (c) The visualization of cosine similarity between raw tokens and distorted tokens. Similarity is lowest at Early Stage 3, indicating a significant impact on cross-level features.

178

179

180

181

182

183

**Screening**, where shallow layers perform a broad, initial scan of the image, with attention scattered to capture raw textures and edges. This is followed by **Stage 2: Local Information Extraction**, where middle layers consolidate these findings; the Outflow becomes shorter, with attention converging on neighboring patches to analyze local features with clear structures. Finally, the deep layers execute **Stage 3: Global Semantic Integration**. In this phase, the model integrates refined local features into a holistic, semantic representation, with attention converging on a few key “summary tokens.” Liu et al. (2025); Li et al. (2023c)

190

191

192

193

To quantitatively validate our three-stage finding, we measure two layer-wise attention distance metrics Dosovitskiy et al. (2020) on 1,000 images from the CC3M dataset Changpinyo et al. (2021): the Average Attention Distance ( $D_{\text{avg}}$ ) and the Average Max Attention Distance ( $D_{\text{top1}}$ ).

$$D_{\text{avg}} = \frac{1}{N} \sum_{i=1}^N \sum_{j=1}^N A_{ij} \cdot d(p_i, p_j), \quad D_{\text{top1}} = \frac{1}{N} \sum_{i=1}^N d(p_i, p_{\text{argmax}_j A_{ij}})$$

197

198

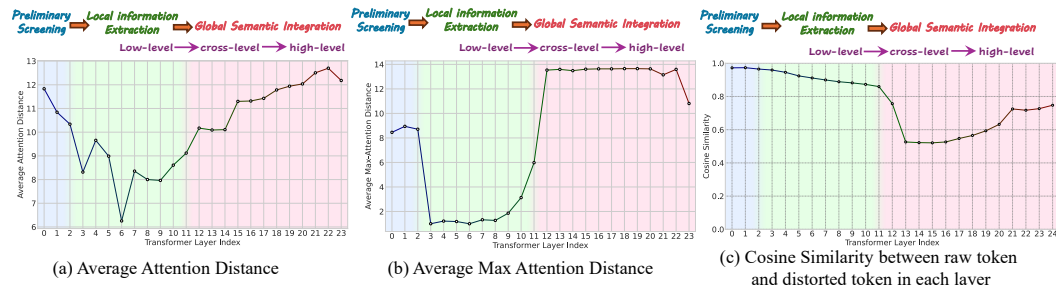
199

200

201

202

Here,  $A$  is the  $NN$  attention map from a self-attention layer, where  $A_{ij}$  is the attention weight from token  $j$  to token  $i$ . The term  $p_i$  denotes the 2D spatial position of the  $i$ -th token in the input image. Consequently,  $d(p_i, p_j)$  represents the Euclidean distance between the positions of tokens  $i$  and  $j$ . As plotted in Fig. 5(a)(b), both metrics exhibit a clear U-shaped trend. The average distance is high during **Stage 1**, decreases for **Stage 2**, and increases again during **Stage 3**. This quantitative trend strongly corroborates our findings.



213

214

215

Figure 5: (a)(b) Attention distance and (c) the impact of distortion on internal tokens in the vision encoder. Low-level (Stage 2) and coarse high-level features (the later phase of Stage 3) are relatively robust to compression artifacts, while cross-level features (the early phase of Stage 3) are significantly affected because they require both high-fidelity low-level details and emerging high-level semantic context. Blue, green, and red indicate stages 1, 2, and 3, respectively.

216 2.2.2 HOW DOES COMPRESSION DISTORTION AFFECT MLLMs?  
217

218 Having established the three-stage information flow model, we analyze its vulnerability to compres-  
219 sion distortion. By measuring the cosine similarity of feature tokens between original and com-  
220 pressed images at each layer, a clear pattern emerges, as shown in Fig. 5(c). While the low-level  
221 features in Stage 1 and 2 prove relatively robust to compression, linearly and slowly decrease in  
222 similarity layer by layer, we observe a sharp drop in similarity in the early phase of Stage 3, which  
223 marks a critical failure in the formation of cross-level features. These features are uniquely vuln-  
224 erable because their creation requires a delicate synthesis of high-fidelity low-level details from Stage  
225 2 and emerging high-level semantic context from Stage 3. Consequently, even the subtle corruption  
226 of the low-level details by compression leads to a disproportionately large failure in this synthesis  
227 process. In contrast, the similarity recovers in the later part of Stage 3, demonstrating that coarse,  
228 high-level semantics are more resilient. This finding is further corroborated by the attention maps,  
229 PCA features and cosine similarity in Fig 4(b)(c). While these visualizations show little change in  
230 PCA features and high cosine similarity in stages 1 and 2 between original and compressed images,  
231 the token similarity in the early phase of stage 3 is significantly decreased. The later part of stage  
232 3 is aimed at generating coarse high-level semantic information. Therefore, the impact of distorted  
233 details is diminished, resulting in a higher overall cosine similarity. As shown in Fig. 2, compres-  
234 sion distortion only minimally affects questions of high-level semantics (e.g., “What is the fruit?”)  
235 or low-level structure (e.g., “What is the word?”). Its impact is much greater, however, on tasks like  
236 counting or texture analysis, which demand both local details and global context.

236 Task-level validation confirms this hypothesis. As shown in Fig. 1(c)(d), tasks requiring the synthe-  
237 sis of both detailed and semantic information (e.g., “count”) degrade severely under compression.  
238 Conversely, tasks reliant on either robust low-level structures (OCR) or coarse high-level semantics  
239 (positional reasoning) remain resilient. This leads to a key insight: **the critical failure point of**  
240 **compression is not a uniform loss of different feature types, but a disproportionate collapse of**  
241 **the cross-level representations that bridge low-level and high-level information.**

242 The takeaways of the above analysis are the following:

243 **Takeaways:**  
244

245 1. *MLLMs require visual information at different levels to perform diverse tasks.*

246 2. *The vision encoder in MLLMs operates in three stages: shallow layers handle initial*  
247 *filtering, middle layers extract low-level features via local analysis, and deep layers perform*  
248 *global semantic integration, sequentially assembling these features into cross-level and then*  
249 *high-level semantic representations.*

250 3. *Compression-induced information loss increases linearly in early layers, indicating that*  
251 *low-level features suffer only modest degradation. However, this compromises cross-level*  
252 *features, which rely on integrating low-level information with high-level context to preserve*  
253 *fine-grained semantics. In contrast, coarse high-level features are moderately affected, as*  
254 *they depend more on abstract representations.*

255 These expose a fundamental paradox in current ICM approaches Kao et al. (2025); Li et al. (2024b);  
256 Chamain et al. (2021). They only try to preserve the high-level information but ignore the low-level  
257 information, which is important for MLLMs to generate cross-level features. Our work is thus built  
258 upon a new cornerstone: **An effective codec must simultaneously preserve proper both low-level**  
259 **fidelity and high-level semantic information.**

260 3 COTAM: CODEC TAILORED TO MLLMs  
261

262 Our analysis reveals a core principle for a codec tailored to MLLMs: it must preserve multi-level  
263 visual information. Based on this principle, we introduce CoTaM, a codec designed with a dual-  
264 strategy approach, as depicted in Fig. 6(b). First, drawing upon the insight from Takeaway 2—that  
265 the initial layers of a vision encoder perform preliminary information filtering—our encoder uses  
266 shallow CLIP attention to guide bitrate allocation, prioritizing important regions for MLLMs. Sec-  
267 ond, inspired by Takeaways 1 and 3, our decoder uses the decompressed image as a reconstruction  
268 prior to retain robust low-level details and avoid domain shift. A latent feature adapter then injects  
269

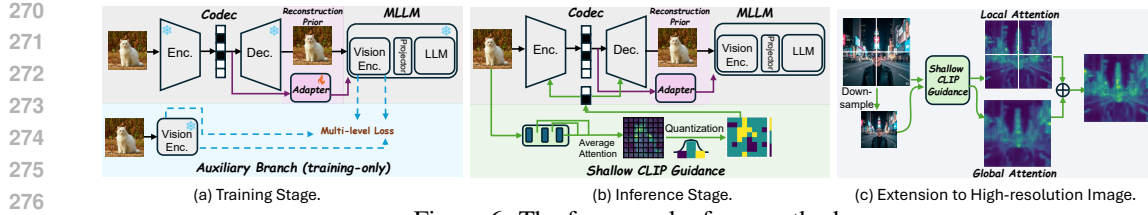


Figure 6: The framework of our method.

semantic enhancements, and the entire model is optimized with a multi-level loss that supervises fidelity at multi-level features. Furthermore, for high-resolution inputs, CoTaM incorporates a Hierarchical Guidance mechanism to fuse multi-scale semantic information, making it compatible with the patch-based processing Liu et al. (2024a) common in MLLMs for both images and videos.

### 3.1 BASE CODEC

Our base codec enables variable bitrates by adapting the multi-quantizer methodology from Jia et al. (2025); Cui et al. (2021). We equip its internal layers with multiple sets of learned quantization vectors for each bitrate to adaptively allocate bits for each spatial location. This allows the semantic importance map to select a specific vector for each region, thereby assigning more bits to critical areas and fewer to the rest areas. Further architectural details are provided in the Appendix.

### 3.2 SHALLOW CLIP-GUIDED ENCODER

Our Shallow CLIP-guided encoder is born from the **Takeaways 2** of our prior analysis: the shallow layers of an MLLM’s vision encoder perform a preliminary screening to identify regions of potential importance. To leverage this early-stage intelligence, we average the [CLS] attention scores from the first three layers of a frozen CLIP model Radford et al. (2021)—chosen for their high attention distance (Fig. 5)—to create a small downsampled spatial map (e.g., 8x8), which quantifies the semantic richness of each region.

This continuous map is subsequently converted into a discrete, three-level mask via a statistics-based quantization method  $\mu \pm k\sigma$ . The three integer levels in this mask directly correspond to rate allocation instructions: decrease bitrate, maintain base bitrate, or increase bitrate. Crucially, due to the small size of this map and its quantization into only three values, the bitrate overhead for this map is negligible (128 bits for 336x336 input). This final mask then directly modulates the quantization parameters of our learned compression backbone on a patch-wise basis, ensuring that semantically critical regions for MLLMs are allocated more bitrate and with higher fidelity.

### 3.3 MULTI-LEVEL FIDELITY DECODER

Our analysis revealed a critical flaw in existing ICM methods: in their pursuit of high-level semantic fidelity, they often degrade the low-level structured information, and also in turn lead to a significant loss of cross-level features. To resolve this problem, our decoder is designed to preserve fidelity across the entire feature hierarchy. It achieves this through two key components:

First, our design leverages the decoded image as a reconstruction prior. This approach serves two critical functions. On the one hand, as shown in Fig. 1 and takeaway 3, since standard compression is already effective at preserving robust low-level structures, using the decoded image ensures this foundational information is retained. On the other hand, it mitigates a potential domain shift, as MLLM vision encoders are pre-trained on natural RGB images; providing the decoded image as a prior grounds the input in the expected domain. Upon this prior, a lightweight **Latent Feature Adapter**, composed of a single transformer block, operates directly on the decoded latent code from the bitstream. It generates a semantic enhancement feature that is fused (via element-wise addition) with the patch embeddings extracted from the decoded image. This strategy injects high-level guidance directly into the feature domain without disrupting the crucial low-level information.

Second, as illustrated in Fig. 6(a), the entire framework is trained end-to-end using a multi-level fidelity loss,  $\mathcal{L}_{\text{total}}$ , to supervise the fidelity at both ends of the feature spectrum. This loss is a

324 weighted sum of two components:

$$\mathcal{L}_{\text{total}} = \lambda_{\text{low}} \mathcal{L}_{\text{low}} + \lambda_{\text{high}} \mathcal{L}_{\text{high}} \quad (1)$$

325 The first component, the **low-level fidelity loss** ( $\mathcal{L}_{\text{low}}$ ), is designed to preserve fine-grained details  
 326 often damaged by existing methods. Guided by our finding in **Takeaway 3**, it imposes critical  
 327 constraints on the shallow layers by minimizing the Mean Squared Error (MSE) between the patch  
 328 embedding features of the original and decoded images. Simultaneously, the **high-level perceptual**  
 329 **loss** ( $\mathcal{L}_{\text{high}}$ ) ensures global semantic coherence by minimizing the MSE between the final-layer token  
 330 representations of the original and our processed output.

### 333 3.4 EXTENSION TO HIGH-RESOLUTION AND VIDEO INPUTS

334 Handling high-resolution images is a critical capability for MLLMs, making it imperative for codecs  
 335 to support them efficiently. This presents a core dilemma. On one hand, guidance from a single,  
 336 fixed-size downsampled image is too coarse; as shown in Fig. 6(c), the background attention is rel-  
 337 atively coarse, failing to focus on important information. A direct strategy to adapt to this, inspired  
 338 by mainstream MLLM processing pipelines, is to employ a patch-based method where local guid-  
 339 ance is applied to each patch independently. The fundamental limitation of this approach, however,  
 340 is its lack of global perception; it cannot determine which local information is crucial for building  
 341 coherent semantics across different patches. For instance, in Fig. 6(c), it lacks sufficient attention on  
 342 the person’s head. Therefore, to resolve this conflict between local detail preservation and global se-  
 343 mantic integrity, we propose our **Hierarchical Guidance** to fuse (via addition) both global and local  
 344 maps, creating a comprehensive guidance signal that is both locally precise and globally aware. On  
 345 the other hand, we resize the decoded high-resolution features to get a global feature before they are  
 346 processed by the adapter. This is done to match the expected input of the high-resolution MLLM,  
 347 which is composed of multiple high-resolution patches and a downsampled global patch.

348 Our method is also compatible with video MLLMs. Current mainstream approaches typically pro-  
 349 cess videos by sampling a sequence of individual frames, a strategy analogous to the patch-based  
 350 processing of high-resolution images. Consequently, our semantic guidance mechanism can be ap-  
 351 plied on a frame-by-frame basis to guide the compression of videos.

## 353 4 EXPERIMENT

### 355 4.1 EXPERIMENTAL SETTINGS

356 **Codec Setting.** Our framework is built upon two learned image compression models, ELIC He  
 357 et al. (2022) and DCAE Lu et al. (2025) to demonstrate the versatility of our approach in being  
 358 integrated with different codecs. For model training, we utilized a dataset comprising one million  
 359 images randomly sampled from the CC3M dataset Changpinyo et al. (2021). The training protocol  
 360 spans a total of five epochs, with the first epoch dedicated to an initialization phase using only the  
 361 low-level fidelity loss ( $\mathcal{L}_{\text{low}}$ ). This pre-training step ensures a stable optimization trajectory by al-  
 362 lowing the network to first grasp the reconstruction of basic structural features. For hyperparameters  
 363  $k$ ,  $\lambda_{\text{low}}$  and  $\lambda_{\text{high}}$ , we empirically set them to 0.75, 0.1, and 1, respectively.

364 **MLLM Setting.** For MLLM evaluation, our primary experiments were conducted on LLaVA-  
 365 1.5 Liu et al. (2024a)(both 7B and 13B variants with a CLIP encoder Radford et al. (2021)) to assess  
 366 performance and scalability. To further substantiate the generalization capabilities of our method,  
 367 we also performed tests on LLaVA-Onevision-7B Li et al. (2024a) (with a SigLIP encoder Zhai et al.  
 368 (2023)) and InternVL2-8B Chen et al. (2024) (with an InternViT encoder Gao et al. (2024)).

369 **Testing Benchmark** Our evaluation protocol is twofold, assessing both MLLM tasks performance  
 370 and image reconstruction quality. For image benchmark, we evaluated on MME Fu et al. (2023),  
 371 TextVQA Singh et al. (2019), POPE Li et al. (2023b), SeedBench Li et al. (2023a), VQAv2 Goyal  
 372 et al. (2017), MMMU Yue et al. (2024), and MMBench Liu et al. (2024b). For video benchmark:  
 373 we used Video-MME Fu et al. (2025). For reconstruction metric, we report PSNR.

374 **Compared Methods** To position our work within the current landscape, we compared the codec  
 375 against a comprehensive set of baselines. For human-centric image compression methods, we se-

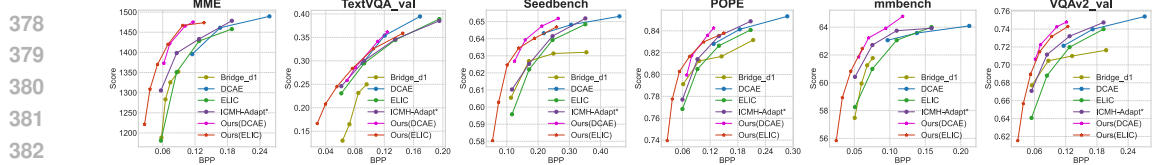


Figure 7: Performance comparison on LLaVA-1.5-7B.

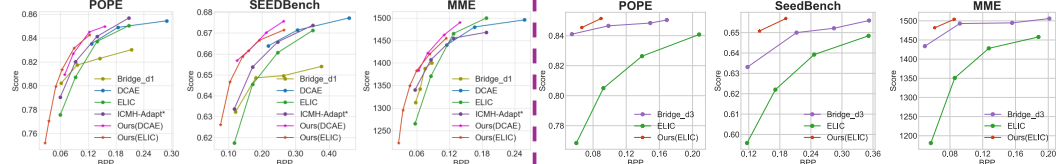


Figure 8: Left three: Performance comparison on LLaVA-1.5-13B. Right three: Performance comparison with methods that fine-tuned the codec encoder.

lected ELIC He et al. (2022), and DACE Lu et al. (2025). For coding for machine methods, we compared against Bridge-d1 (fixing encoder), Bridge-d3 (finetuning encoder) Kao et al. (2025) and ICMH-adapt Li et al. (2024b). Since ICMH-adapt Li et al. (2024b) only supports the ResNet architecture, we reimplemented this method and trained it with our multi-level loss.

## 4.2 PERFORMANCE COMPARISON

### 4.2.1 LOW-RESOLUTION IMAGE BENCHMARK

Our primary validation, presented in Fig. 7, is conducted on the LLaVA-v1.5-7B model with a 336x336 input resolution. Using ELIC as the base codec, our method consistently outperforms previous approaches across six diverse benchmarks. As shown in Table 2, under the same performance level, it achieves a 35.99% bitrate saving. To demonstrate its generalizability, we integrated our method with another SOTA codec, DCAE Lu et al. (2025), and achieved similar performance gains. The scalability of our approach is further validated in Fig. 8, where we also show improvements on the larger LLaVA-1.5-13B model, proving its effectiveness across different model scales.

**Finetuning Codec.** While our main approach freezes the codec to sidestep the performance-reconstruction trade-off, we also test a fine-tuning variant by adding a rate loss Minnen et al. (2018) to the objective (Eq. 1). The results, presented in Fig. 8, show that even in this comparison with another fine-tuning method Kao et al. (2025), our approach demonstrates superior performance. Furthermore, both methods significantly outperform the original, non-fine-tuned base codec.

### 4.2.2 HIGH-RESOLUTION IMAGE AND VIDEO BENCHMARK

Addressing the significant overhead of high-resolution data, we extend our method to this domain. To the best of our knowledge, our work is the first to pioneer a coding framework for high-resolution image and video MLLMs. We validate this on two mainstream models, LLaVA-OneVision-7B and InternVL2-8B, with results presented in Fig. 9. For high-resolution images, our approach consistently outperforms the base codec. Because the current mainstream Video LLM usually extracts video frames into fixed frame images (such as 16, 32 frames), our method can also be directly applied to video MLLM. The codec also achieves superior performance on Video-MME.

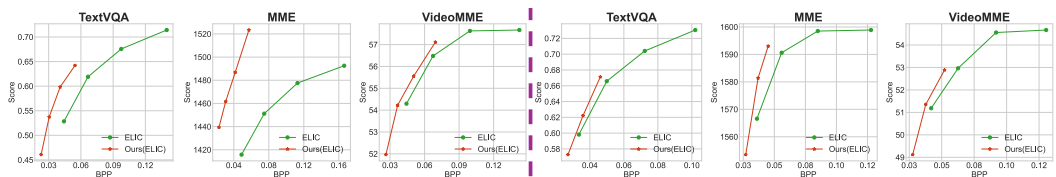


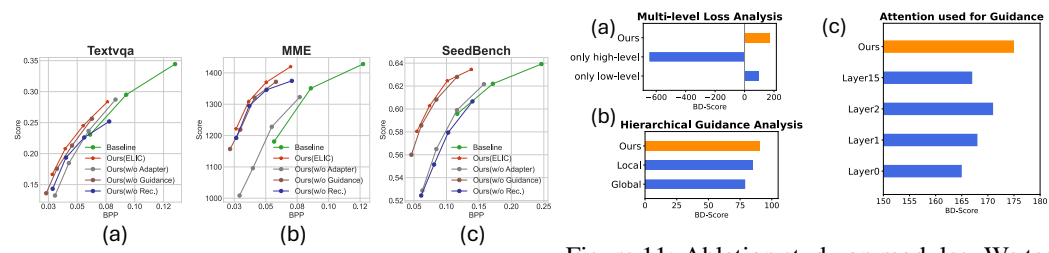
Figure 9: Performance comparison on High-resolution and Video MLLM. Left three: LLaVA-1.5-7B. Right three: InternVL2-8B.

432 4.3 ABLATION STUDY  
433

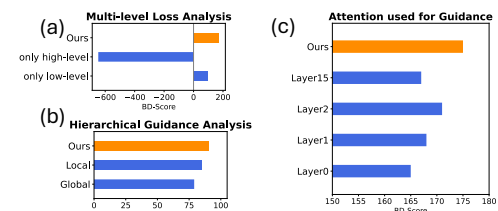
434 **Framework.** To assess each component’s contribution, we perform an ablation study. As shown  
435 in Fig. 10(a)(b)(c), the removal of the Adapter module induces a catastrophic degradation in per-  
436 formance across all three benchmarks. This consistent and vast performance underscores the Adapter’s  
437 role as an essential bridge between the compressed features and the downstream MLLM; its function  
438 in aligning feature spaces is both indispensable and universally critical.

439 Conversely, ablating the image reconstruction module (blue curve) also impacts performance, but  
440 with varying severity across benchmarks, reflecting different dependencies on visual fidelity. For  
441 TextVQA (Fig. 10(a)) and SeedBench (Fig. 10(c)), “Ours (w/o Rec.)” drops sharply relative to the  
442 full model, highlighting the value of reconstruction-induced prior knowledge. In contrast, the impact  
443 on MME (Fig. 10(b)) is much milder.

444 Lastly, removing the clip guidance module (brown curve) consistently reduces performance across  
445 benchmarks, indicating it as an effective general optimization.



446 Figure 10: Ablation study on framework. 447

448 Figure 11: Ablation study on modules. We test  
449 BD-score using ELIC as the anchor on MME. 450

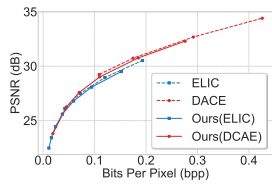
451 **Training Loss.** We validate the necessity of our multi-level loss design. As shown in Fig. 11(a),  
452 relying solely on the high-level loss fails to capture essential low-level details, while using only  
453 the low-level loss produces detailed yet semantically inconsistent results. Optimal performance is  
454 achieved by integrating both.

455 **Hierarchical Guidance.** For high-resolution images, our proposed Hierarchical Guidance im-  
456 proves the importance map by fusing local and global attention. The results in Fig. 11(b) demon-  
457 strate that it yields a clear performance improvement over a purely global guidance strategy.

458 **Attention Maps.** Our use of averaged attention maps from CLIP’s first three layers is validated  
459 in Fig. 11(c), achieving optimal performance as shallow layers are better for holistic screening. In  
460 contrast, deeper layers emphasize global aggregation and thus degrade performance, consistent with  
461 our three-stage information flow model.

470 4.4 COMPLEXITY ANYLSQLS  
471

472 We analyze the computational complexity of our method in Table 2. Since our approach only uti-  
473 lizes the first three shallow layers of the CLIP encoder, the increase in encoding time is marginal  
474 compared to the base codec. Furthermore, as our framework does not require fine-tuning the codec  
475 and the CLIP guidance only reallocates bit rates, the overall PSNR in Fig. 12 shows only a minor  
476 degradation compared to the base codec.

477 Figure 12: PSNR comparison  
478 on Kodak dataset. 479

Method	Encoding (s)	Decoding (s)	Total (s)	BD-Rate $\downarrow$
ELIC	0.173	0.096	0.269	0.00
<b>Ours (ELIC)</b>	0.178 (+2.9%)	0.101 (+5.2%)	0.279 (+3.7%)	<b>-35.99%</b>
DCAE	0.077	0.085	0.162	0.00
<b>Ours (DCAE)</b>	0.080 (+3.9%)	0.091 (+7.1%)	0.171 (+5.6%)	<b>-31.05%</b>

480 Table 2: Comparison of times on Kodak dataset (resized as  
481 336x336), and average BD-rate on six MLLM benchmarks,  
482 which represents the bitrate saved to achieve the same score. 483

486 5 CONCLUSION  
487488 We conduct a comprehensive analysis of how compression artifacts affect MLLMs, revealing that  
489 fine-grained semantic features in cross-level features are highly vulnerable to subtle low-level dis-  
490 tortions. Based on this insight, we propose a codec tailored to MLLMs, featuring CLIP-guided bit  
491 allocation and a multi-level fidelity preserved decoder. Our method consistently achieves significant  
492 bitrate savings while preserving MLLM performance across diverse tasks. This work underscores  
493 the importance of compression strategies aligned with the feature hierarchy of MLLMs.  
494  
495  
496  
497  
498  
499  
500  
501  
502  
503  
504  
505  
506  
507  
508  
509  
510  
511  
512  
513  
514  
515  
516  
517  
518  
519  
520  
521  
522  
523  
524  
525  
526  
527  
528  
529  
530  
531  
532  
533  
534  
535  
536  
537  
538  
539

540 REFERENCES  
541

542 Jinze Bai, Shuai Bai, Yunfei Chu, Zeyu Cui, Kai Dang, Xiaodong Deng, Yang Fan, Wenbin Ge,  
543 Yu Han, Fei Huang, et al. Qwen technical report. *arXiv preprint arXiv:2309.16609*, 2023.

544 Benjamin Bross, Ye-Kui Wang, Yan Ye, Shan Liu, Jianle Chen, Gary J Sullivan, and Jens-Rainer  
545 Ohm. Overview of the versatile video coding (vvc) standard and its applications. *IEEE Transac-*  
546 *tions on Circuits and Systems for Video Technology*, 31(10):3736–3764, 2021.

547 Lahiru D Chamain, Fabien Racapé, Jean Bégaint, Akshay Pushparaja, and Simon Feltman. End-to-  
548 end optimized image compression for machines, a study. In *2021 Data Compression Conference*  
549 (*DCC*), pp. 163–172. IEEE, 2021.

550 Soravit Changpinyo, Piyush Sharma, Nan Ding, and Radu Soricut. Conceptual 12m: Pushing  
551 web-scale image-text pre-training to recognize long-tail visual concepts. In *Proceedings of the*  
552 *IEEE/CVF conference on computer vision and pattern recognition*, pp. 3558–3568, 2021.

553 Yi-Hsin Chen, Ying-Chieh Weng, Chia-Hao Kao, Cheng Chien, Wei-Chen Chiu, and Wen-Hsiao  
554 Peng. Transtic: Transferring transformer-based image compression from human perception to  
555 machine perception. In *Proceedings of the IEEE/CVF International Conference on Computer*  
556 *Vision*, pp. 23297–23307, 2023.

557 Zhe Chen, Weiyun Wang, Yue Cao, Yangzhou Liu, Zhangwei Gao, Erfei Cui, Jinguo Zhu, Shen-  
558 glong Ye, Hao Tian, Zhaoyang Liu, et al. Expanding performance boundaries of open-source  
559 multimodal models with model, data, and test-time scaling. *arXiv preprint arXiv:2412.05271*,  
560 2024.

561 Ze Cui, Jing Wang, Shangyin Gao, Tiansheng Guo, Yihui Feng, and Bo Bai. Asymmetric gained  
562 deep image compression with continuous rate adaptation. In *Proceedings of the IEEE/CVF Con-*  
563 *ference on Computer Vision and Pattern Recognition*, pp. 10532–10541, 2021.

564 Alexey Dosovitskiy, Lucas Beyer, Alexander Kolesnikov, Dirk Weissenborn, Xiaohua Zhai, Thomas  
565 Unterthiner, Mostafa Dehghani, Matthias Minderer, Georg Heigold, Sylvain Gelly, et al. An  
566 image is worth 16x16 words: Transformers for image recognition at scale. *arXiv preprint*  
567 *arXiv:2010.11929*, 2020.

568 Ruoyu Feng, Xin Jin, Zongyu Guo, Runsen Feng, Yixin Gao, Tianyu He, Zhizheng Zhang, Simeng  
569 Sun, and Zhibo Chen. Image coding for machines with omnipotent feature learning. In *European*  
570 *Conference on Computer Vision*, pp. 510–528. Springer, 2022.

571 Chaoyou Fu, Peixian Chen, Yunhang Shen, Yulei Qin, Mengdan Zhang, Xu Lin, Zhenyu Qiu, Wei  
572 Lin, Jinrui Yang, Xiawu Zheng, Ke Li, Xing Sun, and Rongrong Ji. Mme: A comprehensive  
573 evaluation benchmark for multimodal large language models. *ArXiv*, abs/2306.13394, 2023. URL  
574 <https://api.semanticscholar.org/CorpusID:259243928>.

575 Chaoyou Fu, Yuhai Dai, Yongdong Luo, Lei Li, Shuhuai Ren, Renrui Zhang, Zihan Wang, Chenyu  
576 Zhou, Yunhang Shen, Mengdan Zhang, et al. Video-mme: The first-ever comprehensive eval-  
577 uation benchmark of multi-modal llms in video analysis. In *Proceedings of the Computer Vision*  
578 *and Pattern Recognition Conference*, pp. 24108–24118, 2025.

579 Zhangwei Gao, Zhe Chen, Erfei Cui, Yiming Ren, Weiyun Wang, Jinguo Zhu, Hao Tian, Shenglong  
580 Ye, Junjun He, Xizhou Zhu, et al. Mini-internvl: a flexible-transfer pocket multi-modal model  
581 with 5% parameters and 90% performance. *Visual Intelligence*, 2(1):32, 2024.

582 Yash Goyal, Tejas Khot, Douglas Summers-Stay, Dhruv Batra, and Devi Parikh. Making the v in vqa  
583 matter: Elevating the role of image understanding in visual question answering. In *Proceedings*  
584 *of the IEEE conference on computer vision and pattern recognition*, pp. 6904–6913, 2017.

585 Kai Han, Yunhe Wang, Hanting Chen, Xinghao Chen, Jianyuan Guo, Zhenhua Liu, Yehui Tang,  
586 An Xiao, Chunjing Xu, Yixing Xu, et al. A survey on vision transformer. *IEEE transactions on*  
587 *pattern analysis and machine intelligence*, 45(1):87–110, 2022.

594 Dailan He, Ziming Yang, Weikun Peng, Rui Ma, Hongwei Qin, and Yan Wang. Elic: Efficient  
 595 learned image compression with unevenly grouped space-channel contextual adaptive coding. In  
 596 *Proceedings of the IEEE/CVF conference on computer vision and pattern recognition*, pp. 5718–  
 597 5727, 2022.

598 Aaron Hurst, Adam Lerer, Adam P Goucher, Adam Perelman, Aditya Ramesh, Aidan Clark, AJ Os-  
 599 trow, Akila Welihinda, Alan Hayes, Alec Radford, et al. Gpt-4o system card. *arXiv preprint*  
 600 *arXiv:2410.21276*, 2024.

601 Zhaoyang Jia, Bin Li, Jiahao Li, Wenxuan Xie, Linfeng Qi, Houqiang Li, and Yan Lu. Towards  
 602 practical real-time neural video compression. In *Proceedings of the Computer Vision and Pattern*  
 603 *Recognition Conference*, pp. 12543–12552, 2025.

604 Chia-Hao Kao, Cheng Chien, Yu-Jen Tseng, Yi-Hsin Chen, Alessandro Gnutti, Shao-Yuan Lo,  
 605 Wen-Hsiao Peng, and Riccardo Leonardi. Bridging compressed image latents and multimodal  
 606 large language models. In *The Thirteenth International Conference on Learning Representations.*,  
 607 2025.

608 Bo Li, Yuanhan Zhang, Dong Guo, Renrui Zhang, Feng Li, Hao Zhang, Kaichen Zhang, Peiyuan  
 609 Zhang, Yanwei Li, Ziwei Liu, et al. Llava-onevision: Easy visual task transfer. *arXiv preprint*  
 610 *arXiv:2408.03326*, 2024a.

611 Bohao Li, Rui Wang, Guangzhi Wang, Yuying Ge, Yixiao Ge, and Ying Shan. Seed-bench: Bench-  
 612 marking multimodal llms with generative comprehension. *arXiv preprint arXiv:2307.16125*,  
 613 2023a.

614 Han Li, Shaohui Li, Shuangrui Ding, Wenrui Dai, Maida Cao, Chenglin Li, Junni Zou, and Hongkai  
 615 Xiong. Image compression for machine and human vision with spatial-frequency adaptation. In  
 616 *European Conference on Computer Vision*, pp. 382–399. Springer, 2024b.

617 Yifan Li, Yifan Du, Kun Zhou, Jinpeng Wang, Wayne Xin Zhao, and Ji-Rong Wen. Evaluating  
 618 object hallucination in large vision-language models. *arXiv preprint arXiv:2305.10355*, 2023b.

619 Yiran Li, Junpeng Wang, Xin Dai, Liang Wang, Chin-Chia Michael Yeh, Yan Zheng, Wei Zhang,  
 620 and Kwan-Liu Ma. How does attention work in vision transformers? a visual analytics attempt.  
 621 *IEEE transactions on visualization and computer graphics*, 29(6):2888–2900, 2023c.

622 Zhiyuan Li, Yanhui Zhou, Hao Wei, Chenyang Ge, and Jingwen Jiang. Towards extreme image  
 623 compression with latent feature guidance and diffusion prior. *IEEE Transactions on Circuits and*  
 624 *Systems for Video Technology*, 2024c.

625 Zhuoyuan Li, Junqi Liao, Chuanbo Tang, Haotian Zhang, Yuqi Li, Yifan Bian, Xihua Sheng, Xinmin  
 626 Feng, Yao Li, Changsheng Gao, et al. USTC-TD: A test dataset and benchmark for image and  
 627 video coding in 2020s. *IEEE Transactions on Multimedia*, 2025.

628 Haotian Liu, Chunyuan Li, Qingyang Wu, and Yong Jae Lee. Visual instruction tuning. *Advances*  
 629 *in neural information processing systems*, 36:34892–34916, 2023a.

630 Haotian Liu, Chunyuan Li, Yuheng Li, and Yong Jae Lee. Improved baselines with visual instruction  
 631 tuning. In *Proceedings of the IEEE/CVF conference on computer vision and pattern recognition*,  
 632 pp. 26296–26306, 2024a.

633 Jinming Liu, Heming Sun, and Jiro Katto. Learned image compression with mixed transformer-  
 634 cnn architectures. In *Proceedings of the IEEE/CVF conference on computer vision and pattern*  
 635 *recognition*, pp. 14388–14397, 2023b.

636 Yajie Liu, Guodong Wang, Jinjin Zhang, Qingjie Liu, and Di Huang. Unveiling the knowledge  
 637 of clip for training-free open-vocabulary semantic segmentation. In *Proceedings of the AAAI*  
 638 *Conference on Artificial Intelligence*, volume 39, pp. 5649–5657, 2025.

639 Yuan Liu, Haodong Duan, Yuanhan Zhang, Bo Li, Songyang Zhang, Wangbo Zhao, Yike Yuan,  
 640 Jiaqi Wang, Conghui He, Ziwei Liu, et al. Mmbench: Is your multi-modal model an all-around  
 641 player? In *European conference on computer vision*, pp. 216–233. Springer, 2024b.

648 Jingbo Lu, Leheng Zhang, Xingyu Zhou, Mu Li, Wen Li, and Shuhang Gu. Learned image compression  
 649 with dictionary-based entropy model. In *Proceedings of the Computer Vision and Pattern*  
 650 *Recognition Conference*, pp. 12850–12859, 2025.

651 Andrzej Maćkiewicz and Waldemar Ratajczak. Principal components analysis (pca). *Computers &*  
 652 *Geosciences*, 19(3):303–342, 1993.

653 David Minnen, Johannes Ballé, and George D Toderici. Joint autoregressive and hierarchical priors  
 654 for learned image compression. *Advances in neural information processing systems*, 31, 2018.

655 Alec Radford, Jong Wook Kim, Chris Hallacy, Aditya Ramesh, Gabriel Goh, Sandhini Agarwal,  
 656 Girish Sastry, Amanda Askell, Pamela Mishkin, Jack Clark, et al. Learning transferable visual  
 657 models from natural language supervision. In *International conference on machine learning*, pp.  
 658 8748–8763. PmLR, 2021.

659 Amanpreet Singh, Vivek Natarjan, Meet Shah, Yu Jiang, Xinlei Chen, Dhruv Batra, Devi Parikh,  
 660 and Marcus Rohrbach. Towards vqa models that can read. In *Proceedings of the IEEE Conference*  
 661 *on Computer Vision and Pattern Recognition*, pp. 8317–8326, 2019.

662 Gemini Team, Rohan Anil, Sebastian Borgeaud, Jean-Baptiste Alayrac, Jiahui Yu, Radu Soricut,  
 663 Johan Schalkwyk, Andrew M Dai, Anja Hauth, Katie Millican, et al. Gemini: a family of highly  
 664 capable multimodal models. *arXiv preprint arXiv:2312.11805*, 2023.

665 Qwen Team. Qwen2 technical report. *arXiv preprint arXiv:2407.10671*, 2024.

666 Jintao Tong, Wenwei Jin, Pengda Qin, Anqi Li, Yixiong Zou, Yuhong Li, Yuhua Li, and Ruixuan  
 667 Li. Flowcut: Rethinking redundancy via information flow for efficient vision-language models.  
 668 *arXiv preprint arXiv:2505.19536*, 2025.

669 Hugo Touvron, Thibaut Lavril, Gautier Izacard, Xavier Martinet, Marie-Anne Lachaux, Timothée  
 670 Lacroix, Baptiste Rozière, Naman Goyal, Eric Hambro, Faisal Azhar, et al. Llama: Open and  
 671 efficient foundation language models. *arXiv preprint arXiv:2302.13971*, 2023.

672 Gregory K Wallace. The jpeg still picture compression standard. *Communications of the ACM*, 34  
 673 (4):30–44, 1991.

674 Shukang Yin, Chaoyou Fu, Sirui Zhao, Ke Li, Xing Sun, Tong Xu, and Enhong Chen. A survey on  
 675 multimodal large language models. *National Science Review*, 11(12):nwae403, 2024.

676 Xiang Yue, Yuansheng Ni, Kai Zhang, Tianyu Zheng, Ruqi Liu, Ge Zhang, Samuel Stevens,  
 677 Dongfu Jiang, Weiming Ren, Yuxuan Sun, et al. Mmmu: A massive multi-discipline multi-  
 678 modal understanding and reasoning benchmark for expert agi. In *Proceedings of the IEEE/CVF*  
 679 *Conference on Computer Vision and Pattern Recognition*, pp. 9556–9567, 2024.

680 Xiaohua Zhai, Basil Mustafa, Alexander Kolesnikov, and Lucas Beyer. Sigmoid loss for language  
 681 image pre-training. In *Proceedings of the IEEE/CVF international conference on computer vision*,  
 682 pp. 11975–11986, 2023.

683 Jinguo Zhu, Weiyun Wang, Zhe Chen, Zhaoyang Liu, Shenglong Ye, Lixin Gu, Hao Tian, Yuchen  
 684 Duan, Weijie Su, Jie Shao, et al. Internvl3: Exploring advanced training and test-time recipes for  
 685 open-source multimodal models. *arXiv preprint arXiv:2504.10479*, 2025.

686

687

688

689

690

691

692

693

694

695

696

697

698

699

700

701

702 **A APPENDIX**  
703

704	A.1 Related Works . . . . .	14
705	A.2 Benchmark Examples . . . . .	14
706	A.3 Codec Training Strategy . . . . .	15
707	A.4 Visualization of Bit-rate Allocation . . . . .	16
708	A.5 Preliminary Experiments on Finetuning Strategies . . . . .	16
709	A.6 Discussion on the Quantized CLIP Guidance Map . . . . .	17
710	A.7 Discussion on Video MLLM . . . . .	18
711	A.8 Attention Distance of Different Vision Encoders . . . . .	18
712	A.9 ICM Method Task-wise Performance Drop Leaded by Compression Distortion . .	19
713	A.10 Attention Map and PCA Features of Different Layers . . . . .	21
714	A.11 Information Flow of Different Layer . . . . .	21
715	A.12 Analysis on Other Datasets . . . . .	22
716	A.13 LLM Usage . . . . .	22
717		
718		
719		
720		
721		
722		
723		
724		
725		
726		
727		
728		
729		
730		
731		
732		
733		
734		
735		
736		
737		
738		
739		
740		
741		
742		
743		
744		
745		
746		
747		
748		
749		
750		
751		
752		
753		
754		
755		

724 **A.1 RELATED WORKS**725 **A.1.1 MULTIMODAL LARGE LANGUAGE MODELS (MLLMs)**

726 Multimodal Large Language Models (MLLMs), such as LLaVA Liu et al. (2023a), Gemini Team  
727 et al. (2023), and GPT-4o Hurst et al. (2024), have demonstrated remarkable capabilities by aug-  
728 menting Large Language Models (LLMs) with visual perception. These models typically use a  
729 vision encoder (e.g., Clip Radford et al. (2021), SigLip Zhai et al. (2023)) to process images and an  
730 LLM backbone (e.g., LLama Touvron et al. (2023), Qwen Bai et al. (2023)) to perform cross-modal  
731 reasoning. However, the prevailing cloud-edge deployment of MLLMs—hosting powerful models  
732 on servers while capturing data at the edge—presents a significant communication bottleneck. This  
733 challenge motivates our work to develop a compression solution optimized not for human viewing,  
734 but for the unique perceptual needs of MLLMs.

735 **A.1.2 IMAGE COMPRESSION**

736 The fundamental goal of image compression is to minimize the bits required to represent an im-  
737 age—thereby reducing storage and transmission costs—while maintaining sufficient fidelity for its  
738 intended application. Conventional image compression, encompassing both traditional standards  
739 like JPEG and VVC Wallace (1991); Bross et al. (2021), and modern learned methods Liu et al.  
740 (2023b); Lu et al. (2025), is fundamentally optimized for the Human Visual System (HVS) Li et al.  
741 (2025), often by discarding information that is imperceptible to humans but potentially vital for  
742 machine analysis.

743 To bridge the gap created by this human-centric paradigm, the field of Image Coding for Machine  
744 (ICM) emerged. However, the predominant ICM approach Feng et al. (2022); Chen et al. (2023);  
745 Li et al. (2024b) involves tailoring codecs for narrow, specific tasks like object detection or segmen-  
746 tation. However, this task-specificity is fundamentally at odds with the general-purpose nature of  
747 MLLMs. Thus, a critical research gap remains for a compression solution that preserves the full  
748 visual features required by these models.

750 **A.2 BENCHMARK EXAMPLES**

751 To illustrate the diversity of tasks that Multimodal Large Language Models are expected to per-  
752 form, we provide representative examples from two key benchmarks used in our evaluation. Fig. 13  
753 and 14 showcase selected question-answer pairs from the MME Fu et al. (2023) and SEED-Bench Li  
754 et al. (2023a) benchmarks, respectively. These tasks range from object recognition and counting to

756 Optical Character Recognition (OCR). Notably, the OCR examples involve large-font text where  
 757 understanding the overall structure and positional relationships is crucial for correct interpretation.  
 758 Furthermore, the examples highlight the varied question formats MLLMs must address, encompassing  
 759 both binary (Yes/No) judgments and multiple-choice selections. Collectively, these examples  
 760 underscore the necessity for a compression codec to preserve a wide spectrum of visual information—  
 761 from fine-grained details and high-level semantics to the essential structural and positional  
 762 cues required by these diverse tasks. This challenge is a core motivation for our work.

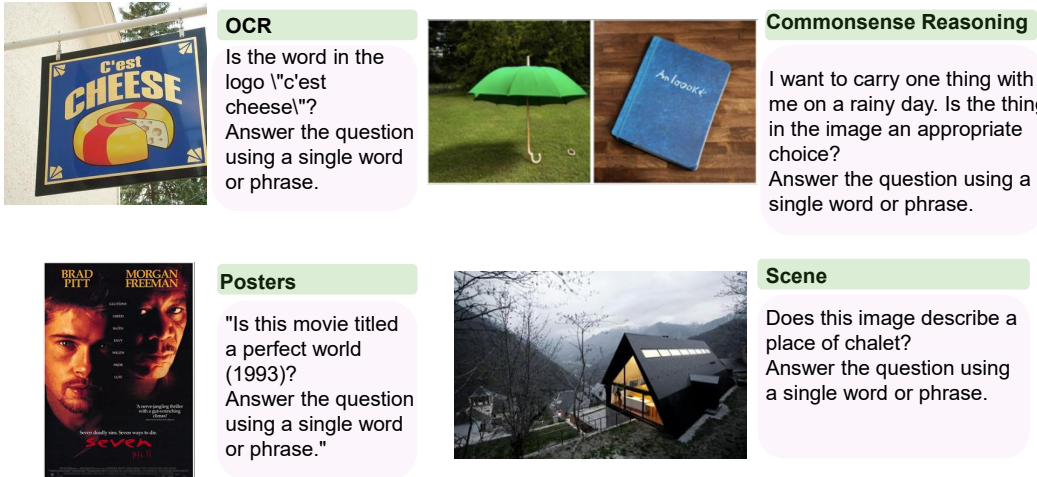


Figure 13: The QA pair examples in MME Benchmark Fu et al. (2023).

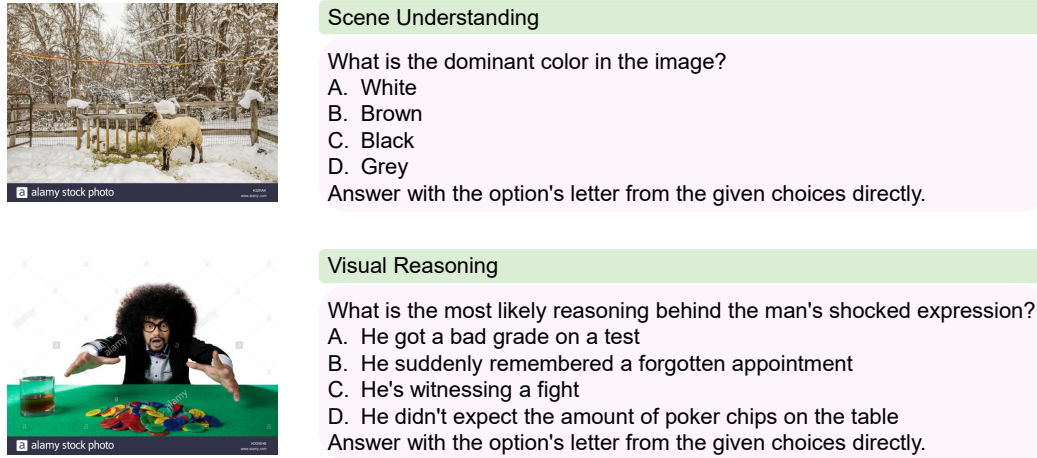


Figure 14: The QA pair examples in SeedBench Benchmark Li et al. (2023a).

### 802 A.3 CODEC TRAINING STRATEGY

803 Following Jia et al. (2025); Cui et al. (2021), our codec is trained to operate at multiple bitrates  
 804 within a single, unified model architecture, as shown in Fig. 15. The core of this variable-rate  
 805 capability lies in the integration of learnable vectors at multiple intermediate layers of the encoder.  
 806 These vectors perform a scaling of the feature maps to dynamically control the information flow  
 807 and, consequently, the final rate-distortion trade-off.

808 Let the feature map at the output of the  $l$ -th encoder layer be denoted as  $f_l$ . For a discrete set of  
 809  $N$  target bitrates  $\mathcal{R} = r_1, r_2, \dots, r_N$ , we introduce  $N$  corresponding sets of learnable vectors. For

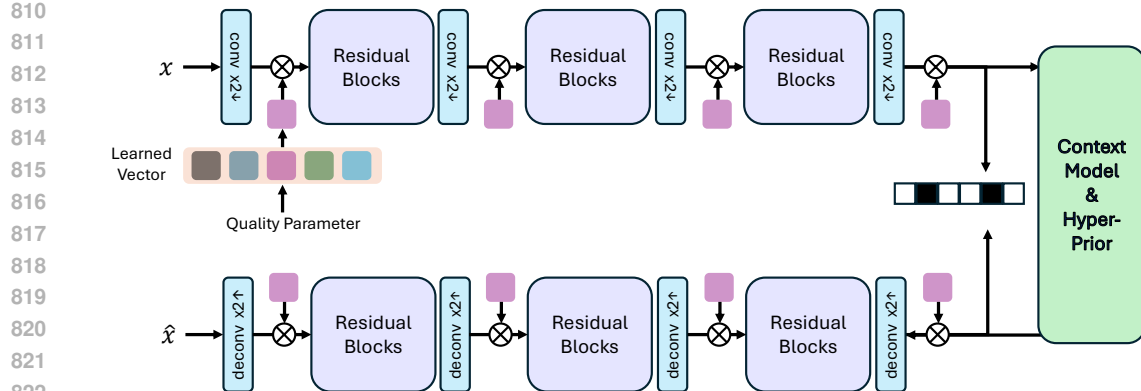


Figure 15: The variable-bitrates compression frameworks.

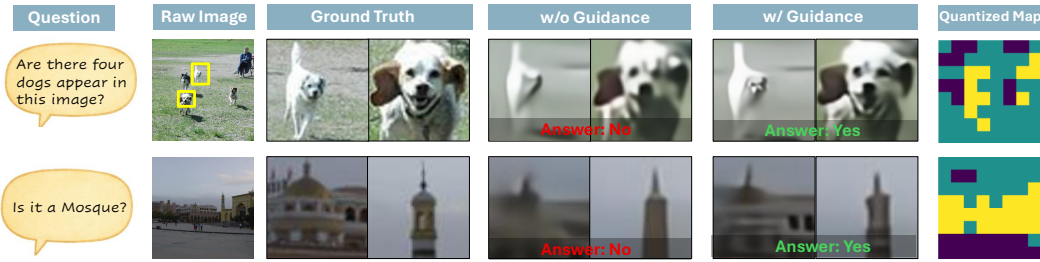


Figure 16: The visualization results under similar total bitrates.

a given target rate  $r \in \mathcal{R}$ , a specific vector  $\mathbf{g}_{l,r}$  is applied to the feature map  $\mathbf{f}_l$  at each modulated layer  $l$ . This operation is formulated as:

$$\mathbf{f}'_l = \mathbf{f}_l \odot \mathbf{g}_{l,r} \quad (2)$$

where  $\odot$  represents element-wise multiplication, and  $\mathbf{f}'_l$  is the scaled feature map that serves as the input to the subsequent layer  $l + 1$ .

During the training process, a quality index  $i$  is randomly sampled in each iteration. This determines both the set of gain vectors  $\mathbf{g}_{l,i}$  to be used in the forward pass and the corresponding trade-off parameter  $\lambda_i$  for the loss function. The entire network, including all  $N$  sets of gain vectors, is optimized end-to-end using the rate-distortion loss:

$$\mathcal{L} = \mathcal{D} + \lambda_i \mathcal{R} \quad (3)$$

where  $\mathcal{D}$  is the distortion loss and  $\mathcal{R}$  is the estimated bit rate. By using a different  $\lambda_i$  for each quality level (where a larger  $\lambda_i$  encourages a lower bitrate). In our implementation, we empirically define  $N = 10$  quality levels, with the corresponding set of tradeoff parameters being  $\lambda_i \in \{0.00002, 0.00005, 0.0001, 0.0002, 0.0004, 0.0008, 0.0016, 0.0032, 0.0064, 0.0128\}$ .

#### A.4 VISUALIZATION OF BIT-RATE ALLOCATION

Fig. 16 visualizes the results of our guidance map’s bit-rate reallocation. It clearly shows that more bits are allocated to semantically important regions, leading to higher fidelity for objects like dogs in the example.

#### A.5 PRELIMINARY EXPERIMENTS ON FINETUNING STRATEGIES

A straightforward strategy to optimize a codec for a MLLM is to directly finetune either the codec or the MLLM on a downstream instruction-following task. To evaluate the efficacy of these approaches, we conducted a set of preliminary experiments. We employed the LLaVA-Instruct dataset Liu et al. (2023a) for finetuning, using a standard cross-entropy loss in MLLM as the optimization objective.

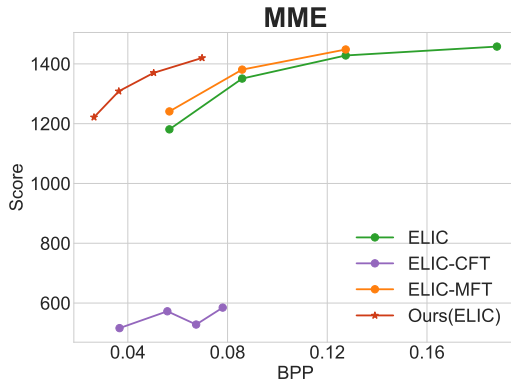


Figure 17: Preliminary experiments on finetuning strategies. ELIC-MFT indicates that the codec parameters are frozen and the MLLM is finetuned. For ELIC-CFT, only the codec parameters are finetuned. Our method only need to finetune the adapter.

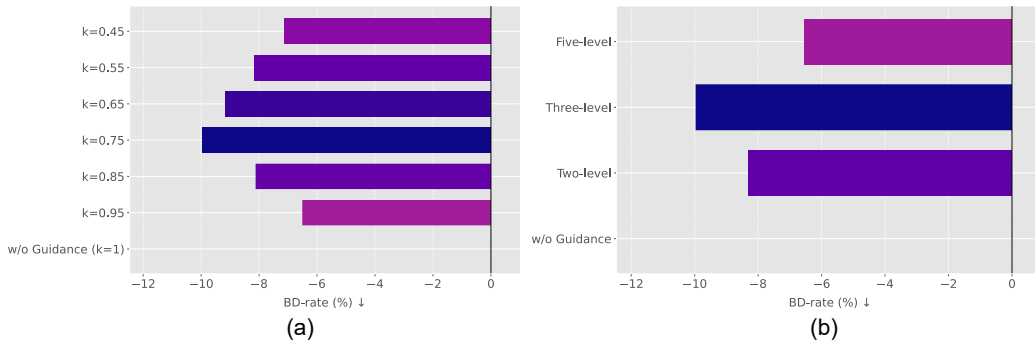


Figure 18: (a) Effect of the statistics-based guidance quantization parameter  $k$  in  $\mu \pm k\sigma$  on BD-rate. All tested values improve over the no-guidance baseline, with performance remaining stable for  $k \in [0.45, 0.85]$ . (b) Impact of the number of quantization levels in the Guidance Quantized Map on BD-rate.

As illustrated in Figure 17, our findings reveal the limitations of direct finetuning. When the codec parameters are frozen and the MLLM is finetuned (ELIC-MFT), we observe only marginal performance gains. More strikingly, when we freeze the MLLM and attempt to finetune the codec (ELIC-CFT), the training process collapses, leading to a catastrophic failure where the model loses its fundamental comprehension abilities. In stark contrast, our proposed method, which only requires finetuning a lightweight adapter, yields substantial performance improvements. These results underscore the inadequacy of direct finetuning and motivate our approach.

## A.6 DISCUSSION ON THE QUANTIZED CLIP GUIDANCE MAP

We explored multiple settings of the Quantized CLIP Guidance Map. First, we examined the statistics-based quantization method  $\mu \pm k\sigma$  with different values of  $k$ . As shown in Fig. 18(a), all  $k$  values yield improvements, and the performance varies only slightly within the range  $k \in [0.45, 0.85]$ . Although we adopt  $k = 0.75$  in the paper, other values within this suitable range produce similar results. Furthermore, as shown in Fig. 18(b), we investigated different numbers of quantization levels. While using multiple levels generally improves performance, the gain diminishes when the spacing between levels becomes large (e.g., the five-level setting), possibly because the wider span assigns overly low quality to some regions, thereby reducing overall performance.

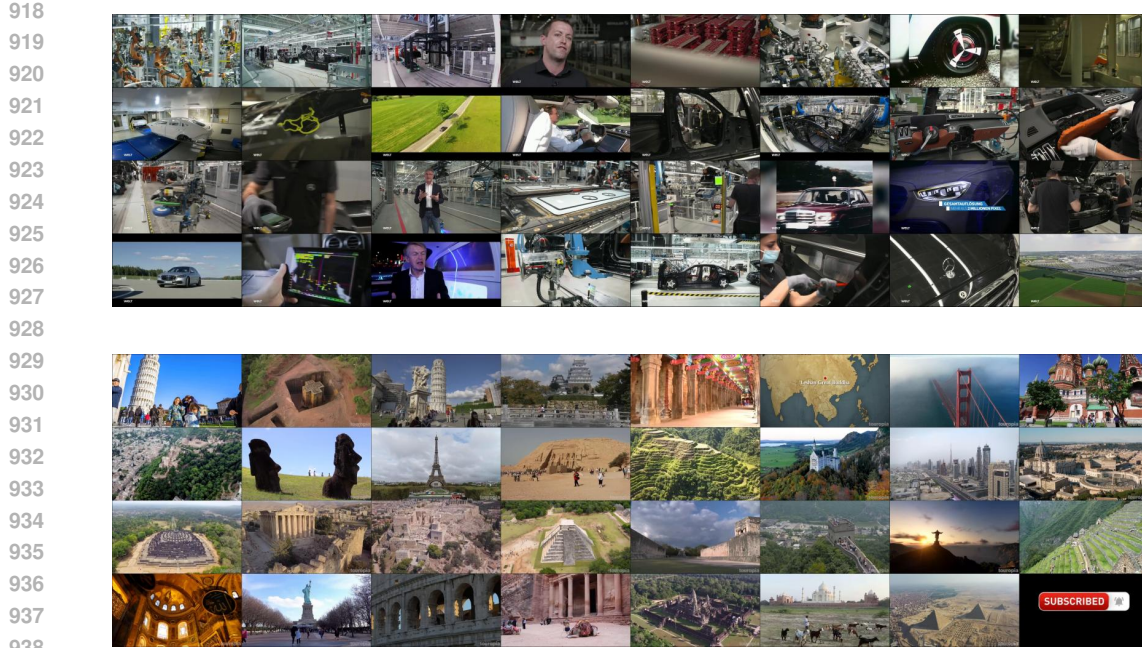


Figure 19: The input examples of video MLLM.

#### A.7 DISCUSSION ON VIDEO MLLM

Our method is also directly applicable to video MLLMs. We note that current mainstream video MLLMs, such as Li et al. (2024a); Chen et al. (2024); Zhu et al. (2025); Hurst et al. (2024), typically operate not on dense video streams, but on a sparsely sampled sequence of keyframes (e.g., 16 or 32 frames extracted from the entire video), as shown in Fig. 19. This sparse sampling strategy inherently reduces the temporal redundancy between adjacent processed frames. Therefore, applying our image codec on a frame-by-frame basis is a practical and well-aligned strategy for this specific application. Consequently, our semantic guidance mechanism can be effectively applied to each sampled frame to guide the compression. While developing a more advanced video codec that explicitly models the remaining long-range temporal correlations presents a valuable direction for future work, our current intra-frame approach offers a strong and pragmatic baseline for compressing visual inputs for today’s video MLLMs.

#### A.8 ATTENTION DISTANCE OF DIFFERENT VISION ENCODERS

To validate that our three-stage information flow model is a general principle rather than an artifact of a specific architecture, we extend our analysis to other prominent vision encoders, namely InternViT Chen et al. (2024) in InternVL2 and SigLIP Zhai et al. (2023) in LLaVA-Onevision Li et al. (2024a). As shown in Fig. 20, the average attention distance per layer for both encoders exhibits a clear U-shaped trend, mirroring the pattern observed with the CLIP encoder in our main analysis. This corroborates our finding that vision encoders broadly follow a three-stage process: an initial broad screening (Stage 1), followed by localized feature extraction (Stage 2), and concluding with global semantic integration (Stage 3). Furthermore, Fig. 21 reveals that the feature similarity under compression shows a sharp drop during the early phase of Stage 3, followed by a recovery in the final layers. This behavior is consistent with our three-stage theory: the initial drop highlights the vulnerability of cross-level features during the synthesis of local details and emerging global context, while the subsequent rebound indicates the formation of a more stable, abstract semantic representation. Notably, SigLIP exhibits two sharp drops in similarity. We hypothesize this is due to SigLIP’s architecture, which lacks a dedicated class token. Consequently, its deeper layers may need to retain some local information for the final pooling process, leading to a lower overall feature similarity. Nevertheless, the feature similarity in SigLIP’s final layer still rebounds, which remains consistent with the global semantic integration phase of the three-stage process.

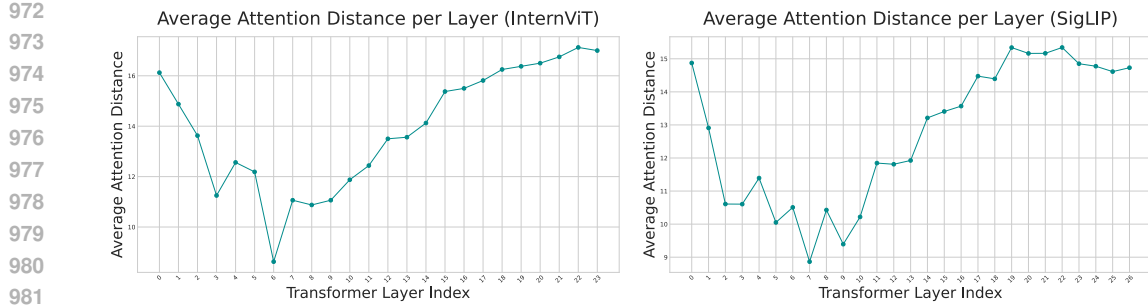


Figure 20: The average attention distance per layer of different vision encoder (InternViT and SigLIP).

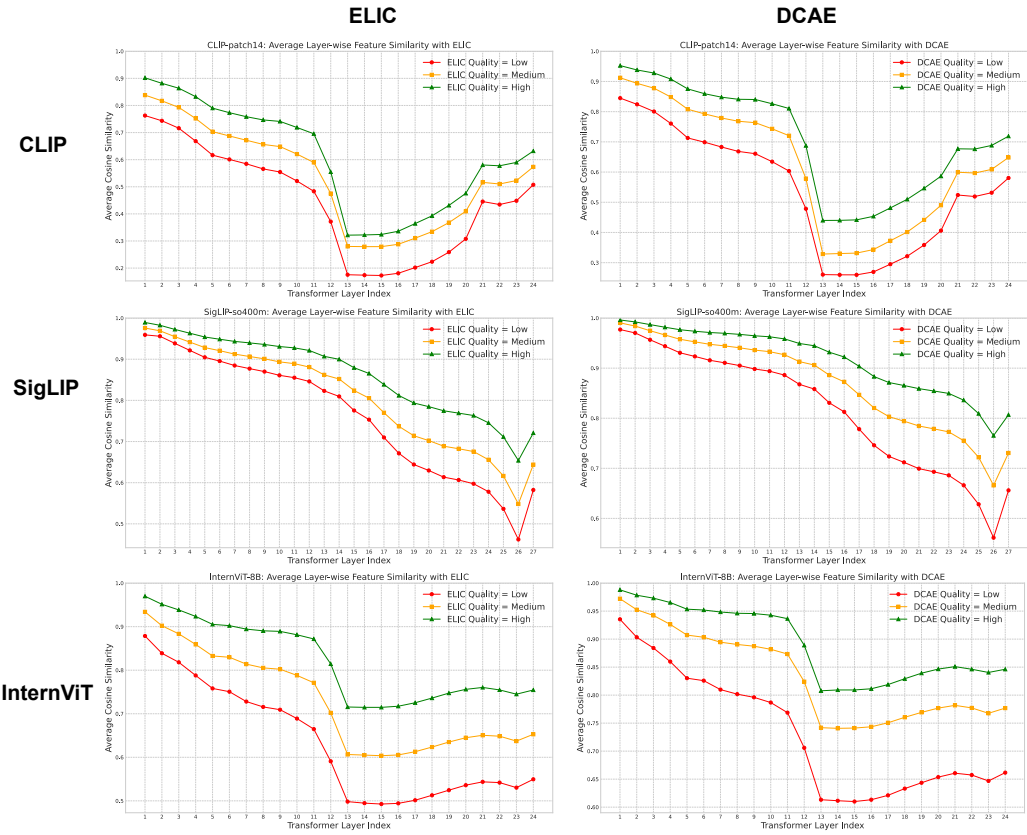


Figure 21: The impact (token similarity) of distortion on internal tokens in the vision encoder.

### A.9 ICM METHOD TASK-WISE PERFORMANCE DROP LEADED BY COMPRESSION DISTORTION

To provide a more granular view of the inconsistent performance of existing codecs, we present a detailed task-wise breakdown of the performance degradation caused by compression. Fig. 22 shows the impact of ELIC, a codec optimized for human perception, on various sub-tasks within the MMBench benchmark. Fig. 23 further illustrates the performance drop on both MME and MM-Bench when using Bridge-d1, an Image Coding for Machine (ICM) method. These figures highlight that both human-centric and machine-centric codecs exhibit erratic performance, excelling in some task categories while failing significantly in others. This inconsistency reinforces the argument that a new paradigm is needed—one that is holistically tailored to the multi-level feature requirements of general-purpose MLLMs.

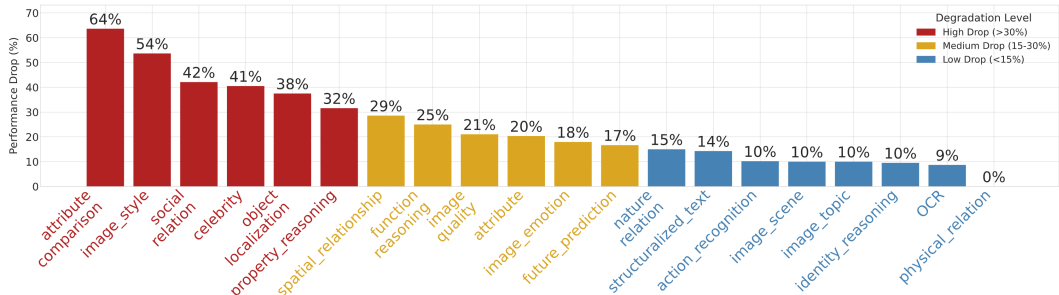
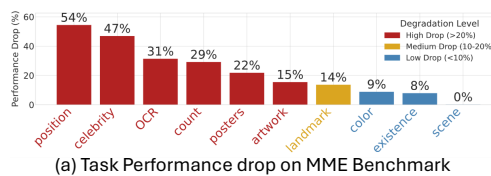


Figure 22: The task-wise impact of compression distortion (from ELIC) on MMBench.



(a) Task Performance drop on MME Benchmark

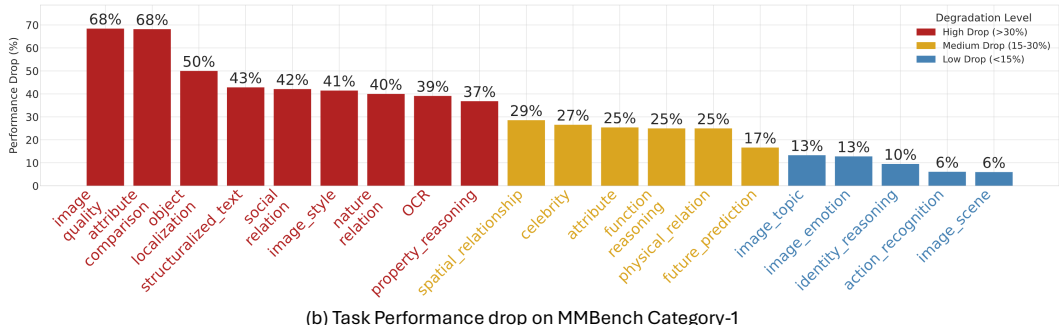


Figure 23: The task-wise impact of compression distortion (from ICM method Bridge-d1) on MME and MMBench.

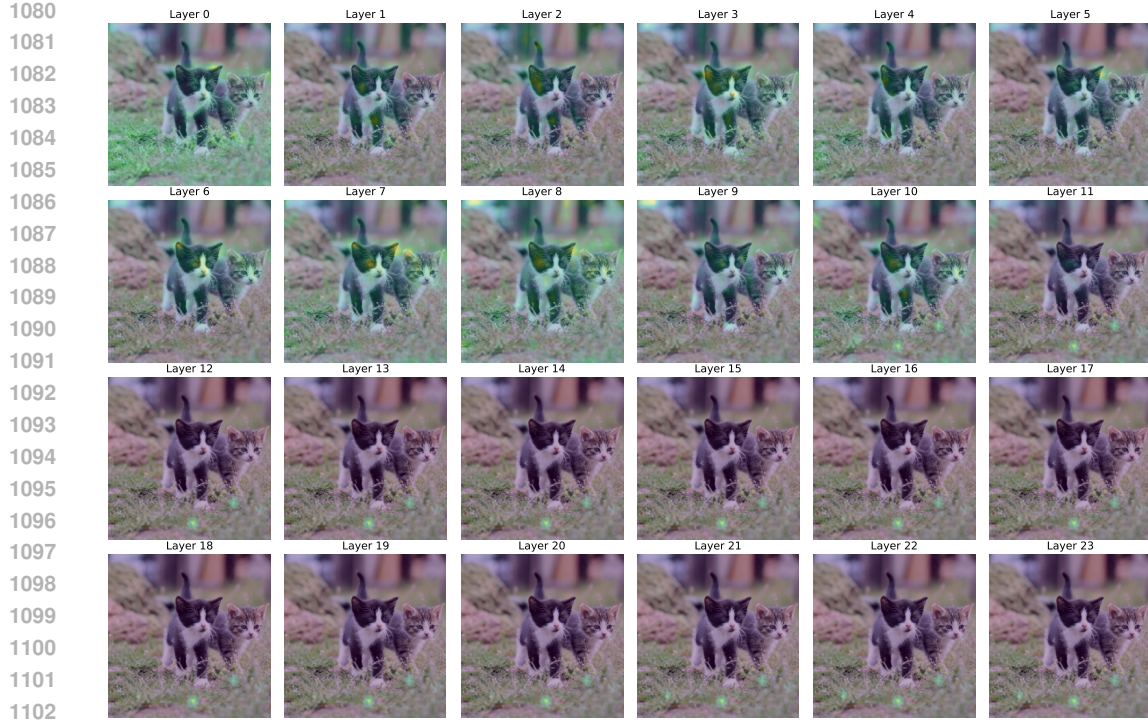


Figure 24: The attention maps of the class token in different layers.

### A.10 ATTENTION MAP AND PCA FEATURES OF DIFFERENT LAYERS

Fig. 24 provides a visual walkthrough of the [CLS] token’s attention maps at different layers of the vision encoder, substantiating our three-stage model. In the shallow layers (Stage 1, e.g., layer 0), the attention is broad and scattered, performing a preliminary screening of the entire image. As we move to the middle layers (Stage 2, e.g., layer 7), attention becomes more focused, converging on local regions and edges to extract structured features. Finally, in the deep layers (Stage 3, e.g., layer 22), the attention disperses again as the model integrates globally aggregated information, with focus shifting to a few “summary tokens” that encapsulate high-level semantic concepts.

Complementing this, the Principal Component Analysis (PCA) visualizations in Fig. 25 reveal the evolution of the features themselves. Features in the shallow layers resemble raw textures and edges. In the middle layers, these evolve into clearly structured local features. By the time we reach the deep layers, the structural details are largely discarded in favor of abstract, high-level semantic representations. Together, the attention patterns and the feature visualizations provide strong, complementary evidence for the distinct information processing stages within the vision encoder.

### A.11 INFORMATION FLOW OF DIFFERENT LAYER

To further dissect the information processing dynamics, we analyze the inflow and outflow patterns for tokens across different layers, as illustrated in Fig. 26. This analysis reveals a clear three-stage progression. Initially, in Stage 1, tokens exhibit wide-ranging inflow and outflow without a clear focus, a pattern characteristic of a broad initial screening of the image. Subsequently, Stage 2 is marked by an asymmetric information flow: inflow remains anchored to the global [CLS] token for guidance, while outflow becomes highly localized to neighboring patches, reflecting a focus on structured local feature extraction. Finally, in Stage 3, the dynamics shift again as most tokens receive targeted inflow from a few “summary” tokens, which in turn broadcast their globally-integrated semantic knowledge via global outflow. This dynamic confirms the final phase of semantic synthesis and integration.

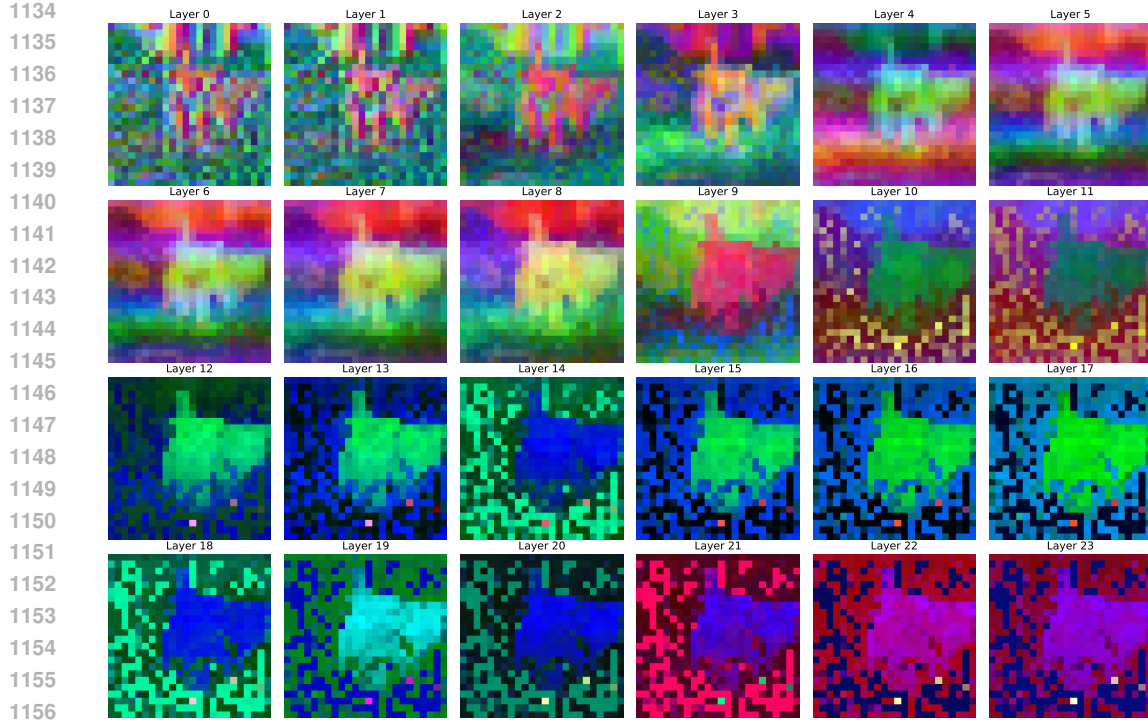


Figure 25: The PCA features in different layers.

## A.12 ANALYSIS ON OTHER DATASETS

In Fig. 27, we present the results obtained from analyzing different datasets. It can be observed that the general curve trends are consistent with those in Fig. 5, indicating that different datasets do not affect our conclusion.

## A.13 LLM USAGE

We acknowledge the use of a large language model (LLM) to assist in the preparation of this manuscript. The LLM's role was strictly limited to improving grammar and refining language. It did not contribute to any of the core research components, such as the initial ideas, experimental design, data analysis, or interpretation of the results.

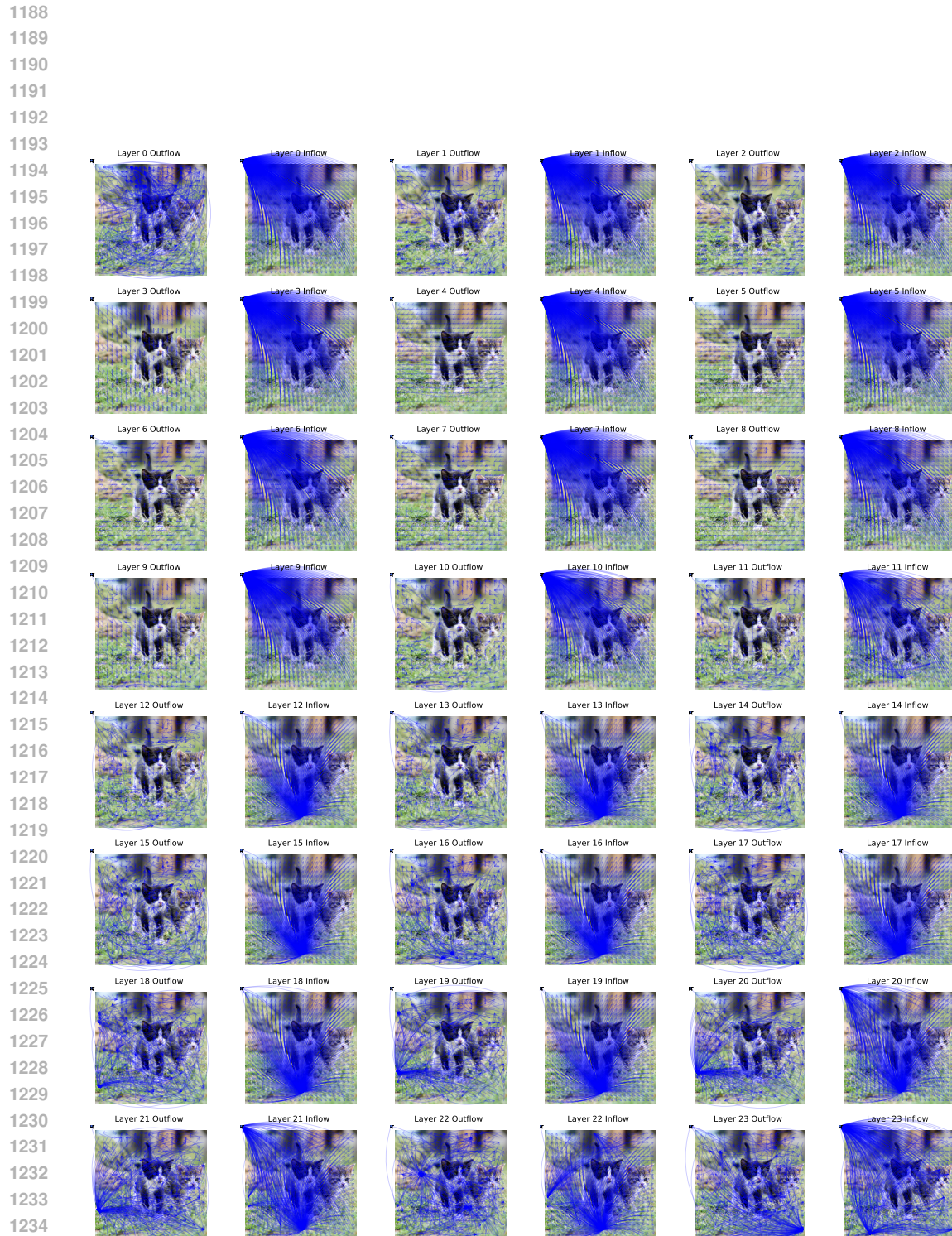


Figure 26: The information flows of different layers.

1242  
 1243  
 1244  
 1245  
 1246  
 1247  
 1248  
 1249  
 1250  
 1251  
 1252  
 1253  
 1254  
 1255  
 1256  
 1257  
 1258  
 1259  
 1260  
 1261  
 1262  
 1263



(a) Kodak



(b) COCO

Figure 27: The attention distance on different datasets.

1272  
 1273  
 1274  
 1275  
 1276  
 1277  
 1278  
 1279  
 1280  
 1281  
 1282  
 1283  
 1284  
 1285  
 1286  
 1287  
 1288  
 1289  
 1290  
 1291  
 1292  
 1293  
 1294  
 1295